

Graphene Mode-Locked Ultrafast Laser

Zhipei Sun,[†] Tawfique Hasan,[†] Felice Torrisi,[†] Daniel Popa,[†] Giulia Privitera,[†] Fengqiu Wang,[†] Francesco Bonaccorso,[†] Denis M. Basko,[‡] and Andrea C. Ferrari^{†,*}

[†]Department of Engineering, University of Cambridge, Cambridge CB3 0FA, U.K. and [‡]LPMCMC, Université Joseph Fourier and CNRS, Grenoble, France

Ultrafast laser sources have many potential applications, ranging from basic research and metrology to telecommunications, medicine, and materials processing.^{1–3} The majority of ultrashort lasers employ a mode-locking technique, whereby a nonlinear optical element, called saturable absorber, turns the laser continuous wave output into a train of ultrashort optical pulses. Semiconductor saturable absorber mirrors (SESAMs) currently dominate passive mode-locking.^{2,4,5} However, these have a narrow tuning range (tens of nanometers) and require complex fabrication and packaging.² A simpler and cost-effective alternative relies on single-walled carbon nanotubes (SWNTs),^{6–10} where the working wavelength is defined by choosing the SWNT diameter (*i.e.*, band gap).^{6,7} Tunability is possible by using a wide diameter distribution.⁸ However, when operating at a particular wavelength, the SWNTs not in resonance are not used and give insertion losses, compromising device performance. Novel nonlinear materials with broadband absorption are therefore required for wideband, tunable operation.

The linear dispersion of the Dirac electrons in graphene offers the ideal solution:¹¹ for any excitation, there will always be an electron–hole pair in resonance. Due to the ultrafast carrier dynamics^{12–14} and large absorption of incident light per layer ($\alpha_1 = 2.3\%$ ^{15,16}), graphene should behave as a fast saturable absorber over a wide spectral range. Compared to SESAMs and SWNTs, graphene saturable absorbers would not need band gap engineering or chirality/diameter control to optimize device performance. Here, we demonstrate an ultrafast fiber laser mode-locked at 1.5 μm , the most common optical telecommunica-

ABSTRACT Graphene is at the center of a significant research effort. Near-ballistic transport at room temperature and high mobility make it a potential material for nanoelectronics. Its electronic and mechanical properties are also ideal for micro- and nanomechanical systems, thin-film transistors, and transparent and conductive composites and electrodes. Here we exploit the optoelectronic properties of graphene to realize an ultrafast laser. A graphene–polymer composite is fabricated using wet-chemistry techniques. Pauli blocking following intense illumination results in saturable absorption, independent of wavelength. This is used to passively mode-lock an erbium-doped fiber laser working at 1559 nm, with a 5.24 nm spectral bandwidth and ~ 460 fs pulse duration, paving the way to graphene-based photonics.

KEYWORDS: graphene · laser · ultrafast optics · composites

tions wavelength, using single-layer graphene (SLG) and few-layer graphene (FLG) flakes.

RESULTS AND DISCUSSION

Graphene Mode-Locker. For ease of integration and stability, we incorporate the flakes into a host polymer. For composite preparation, we exfoliate natural graphite in water without functionalization under mild sonication.^{17,18} This retains the electronic structure of pristine graphene in the exfoliated SLG and FLG flakes.^{17,18} We employ bile salts in order to obtain a stable, higher concentration of SLG and FLG than in previous nonaqueous dispersions.¹⁷ These amphiphilic molecules, with a hydrophobic and a hydrophilic side,¹⁹ disperse graphene by physical adsorption on its surface. In contrast to linear chain surfactants, for example, sodium dodecylbenzene sulfonate (SDBS) widely used for SWNTs, the flat molecular structure of sodium deoxycholate (SDC), used here, efficiently disperses SLG, FLG, and graphitic flakes. Polyvinyl alcohol (PVA) is chosen as host polymer for its mechanical properties and solvent compatibility. The dispersions are mixed with PVA in a polymer mixer. The solvent is then

*Address correspondence to acf26@eng.cam.ac.uk.

Received for review November 26, 2009 and accepted January 8, 2010.

Published online January 25, 2010.
10.1021/nn901703e

© 2010 American Chemical Society

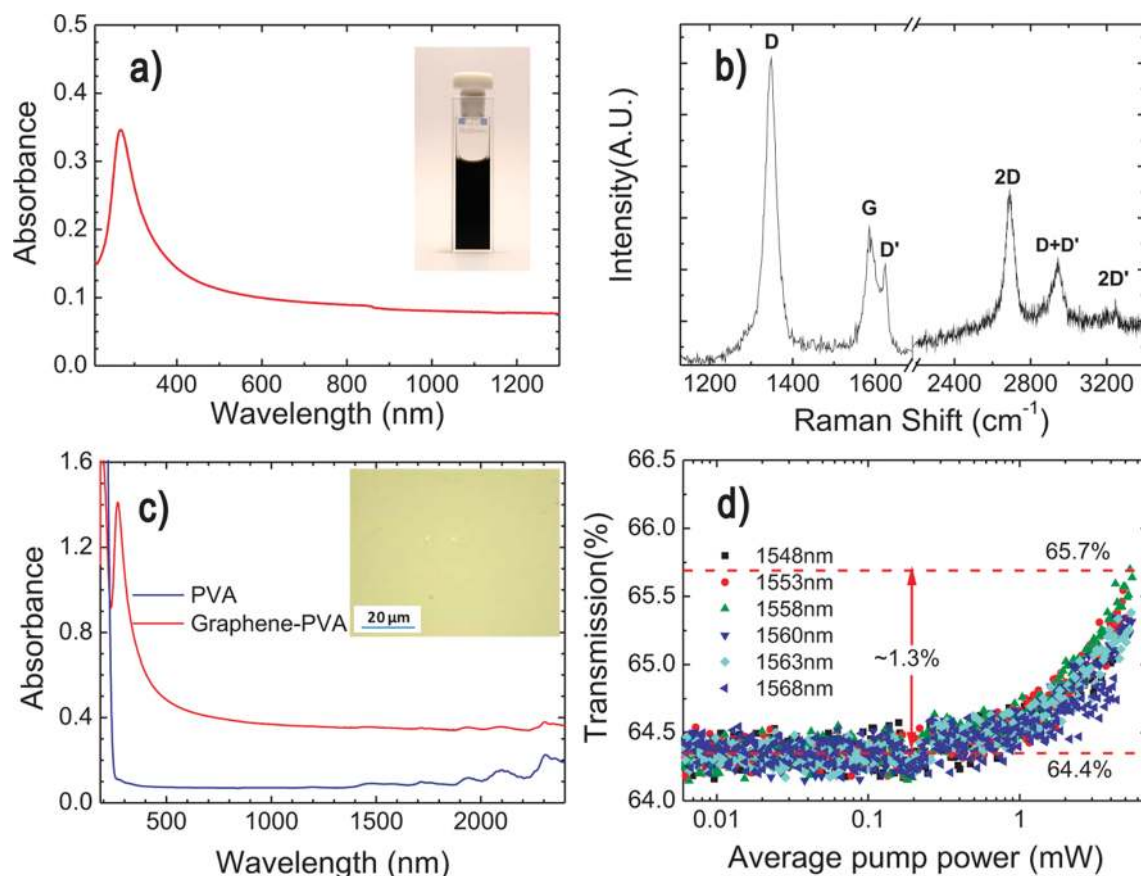


Figure 1. (a) Absorption spectrum of a stable, 10% diluted, graphene dispersion. The inset shows a photograph of the undiluted dispersion. (b) Raman spectrum measured at 514.5 nm for a representative flake. (c) Absorption spectra of graphene–PVA composite and a reference PVA film. Inset: micrograph of a graphene–PVA composite. (d) Typical transmission of the composite as a function of average pump power for six excitation wavelengths.

evaporated to obtain $\sim 50 \mu\text{m}$ thick composites. This simple, wet-chemistry approach is scalable and, more importantly, allows easy integration into a range of photonic systems (see Methods).

We first characterize the dispersions obtained from ultrasonication, followed by centrifugation to remove large residual graphitic particles. Since we need to integrate our composites in transmissive mode in a laser cavity, flakes with dimensions $>1 \mu\text{m}$ are removed to avoid scattering losses.²⁰ Figure 1a shows a photograph of a dispersion after centrifugation and its absorption spectrum. This is mostly featureless, as expected.^{15–18,21–23} The peak in the UV region is a signature of the π plasmon.²⁴ Using the experimental absorption coefficient $1390 \text{ L g}^{-1} \text{ m}^{-1}$ at 660 nm ,^{17,18} we estimate $\sim 0.08 \text{ g/L}$ of graphitic material in the centrifuged dispersion.

The decanted dispersion mostly contains submicrometer flakes. A typical Raman spectrum measured at 514.5 nm is plotted in Figure 1b. Besides the G and 2D peaks, this has significant D and D' intensities and the combination mode D + D' at $\sim 2950 \text{ cm}^{-1}$. The G peak corresponds to the E_{2g} phonon at the Brillouin zone center. The D peak is due to breathing modes of sp^2 rings and requires a defect for its activation by

double resonance (DR).^{25–28} The 2D peak is the second order of the D peak. This is a single band in SLG, whereas it splits in four in bilayer graphene, reflecting the evolution of the band structure.²⁵ The 2D peak is always seen, even when no D peak is present, because no defects are required for the activation of two phonons with the same momentum, one backscattering from the other. DR can also happen as intravalley process, that is, connecting two points belonging to the same cone around **K** or **K'**. This gives rise to the D' peak. The 2D' is the second order of the D' peak. The very large intensity of the D peak in Figure 1b is not due to the presence of a large amount of structural defects, otherwise it would be much broader, and G, D' would merge in a single band.^{26,27} We rather assign it to the edges of the submicrometer flakes we produce.²⁹ We note that the 2D band, although broader than in pristine graphene,²⁵ is still fitted by a single Lorentzian line shape. This implies that, even if the flakes are multilayers, they are electronically almost decoupled and behave, to a first approximation, like a collection of single layers, retaining the Dirac fermions linear dispersion.³⁰

The micrograph of the composite shown in the inset of Figure 1c confirms the homogeneous distribu-

tion of the flakes. This is vital to reduce Mie scattering that could be caused by flakes of dimensions comparable to 1.5 μm , the device operation wavelength.²⁰ The absorption spectra of the graphene–PVA composite and a reference PVA film are presented in Figure 1c. The absorption of the flakes is featureless with the characteristic UV plasmon peak, while the host polymer only contributes a small background for longer wavelengths.

Saturable Absorption. Figure 1d plots the measured transmission as a function of average pump power at six different wavelengths (using a probe laser with pulse width 580 fs, as detailed in Methods). At a relatively low input power level, the transmission, τ , is almost independent of pump power. However, τ increases by $\Delta\tau = 1.3\%$ due to absorption saturation when the incident average power is raised to 5.35 mW (corresponding to a power density of 266 MW/cm²) at 1558 nm. Further increase in transmission is feasible but limited to our maximum available pump intensity. The saturable absorption of the composite is clear for all pump wavelengths. This indicates that our composite can be used over a broad spectral range, unlike SESAMs.² The transmission change is similar to SESAMs.² The nonsaturable insertion loss (34.3%) is larger than that of SESAMs² but comparable to SWNTs.⁸ Note that, for fiber lasers with a relatively large single round-trip gain coefficient, such nonsaturable losses are tolerable.⁸ Further decrease in the nonsaturable insertion loss is expected when the device is completely saturated. To estimate the nonsaturable loss due to the linear coupling between the two fiber connectors, a reference PVA composite $\sim 50\ \mu\text{m}$ thick is used in place of the graphene–PVA composite. The transmission of the packaged pure PVA is $\tau_0 = 82.6\%$. Given the pulse repetition rate of 38.83 MHz, we can then estimate the density of photons absorbed per pulse at our maximum pump power to be $2.3 \times 10^{14}\ \text{cm}^{-2}$. The average number of layers N participating in the absorption process is estimated from $\tau = \tau_0(1 - \alpha_1)^N$, where $\alpha_1 = 2.3\%$ is the absorption per layer, yielding $N \sim 11$ (see Methods). Thus, the density of photons absorbed per pulse per layer is $2.2 \times 10^{13}\ \text{cm}^{-2}$, and $\Delta\tau = 1.3\%$ translates into a relative change in the absorption per layer $\Delta\alpha_1/\alpha_1 = -8.2\%$.

To understand the origin of the observed saturation and give its theoretical estimate, let us discuss the photoexcited carrier kinetics in graphene (Figure 2). Optical interband excitation in SLG and FLG by an ultrashort optical pulse produces a nonequilibrium carrier population in the valence and conduction bands. In time-resolved experiments,^{12,31} two relaxation time scales are typically seen. A fast one, ~ 100 fs, usually associated with carrier–carrier intraband collisions and phonon emission, and a slow one, on a picosecond scale, corresponding to electron interband relaxation and cooling of hot phonons.^{31,32} Several points should be noted here. (i) In our experiment, SLG and FLG flakes

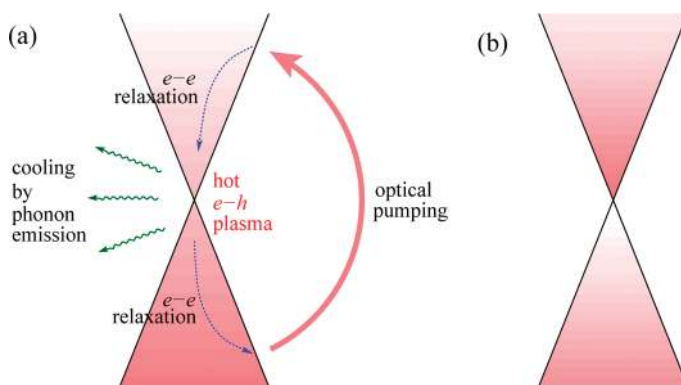


Figure 2. Schematic illustration of photoexcited electron kinetics in graphene. The intensity of the color shading represents the electron population, in the case of (a) efficient interband relaxation and (b) inefficient interband relaxation.

are incorporated in a polymer matrix, so we assume graphene phonons to efficiently give away their energy to the matrix and neglect hot phonon effects. (ii) The rate of carrier–carrier collisions grows with carrier density (*i.e.*, pump power). We assume the collisions to be very fast. (iii) Carrier–carrier collisions preserve the total electronic energy and thus cannot change the effective electronic temperature.

A quantitative treatment of the electron–hole dynamics would require the solution of the kinetic equation for electron and hole distribution functions $f_e(\mathbf{p})$ and $f_h(\mathbf{p})$, \mathbf{p} being the momentum counted from the Dirac point. Here we present an estimate. Let us assume that relaxation times are shorter than the pulse duration, so during the pulse the electrons reach a stationary state, that collisions put electrons and holes in thermal equilibrium at an effective temperature T_{eff} , and that the samples are undoped. Then:

$$f_e(\mathbf{p}) = f_h(\mathbf{p}) = \frac{1}{e^{vp/T_{\text{eff}}} + 1} \quad (1)$$

where v is the Dirac electrons velocity in SLG. The populations determine electron and hole densities $n_{e,h}$ and total energy density \mathcal{E} (counted from the energy of the undoped sample at zero temperature):

$$n_{e,h} = 4 \int \frac{d^2\mathbf{p}}{(2\pi)^2} f_{e,h}(\mathbf{p})$$

$$\mathcal{E} = 4 \int \frac{d^2\mathbf{p}}{(2\pi)^2} vp [f_e(\mathbf{p}) + f_h(\mathbf{p})] \quad (2)$$

the factor 4 accounts for valley and spin degeneracy. The populations also determine the reduction of photon absorption per layer for given laser energy, E_L , due to Pauli blocking, by a factor $1 + \Delta\alpha_1/\alpha_1 = [1 - f_e(\mathbf{p})][1 - f_h(\mathbf{p})]$. In our measurements, $vp = E_L/2 = 0.4$ eV and $1 + \Delta\alpha_1/\alpha_1 \sim 0.92$, implying $T_{\text{eff}} \sim 0.13$ eV.

To obtain a theoretical estimate for T_{eff} , let us assume that during the pulse electrons and holes are injected at the energy $\varepsilon_{\text{in}} = E_L/2 = 0.4$ eV at a constant rate

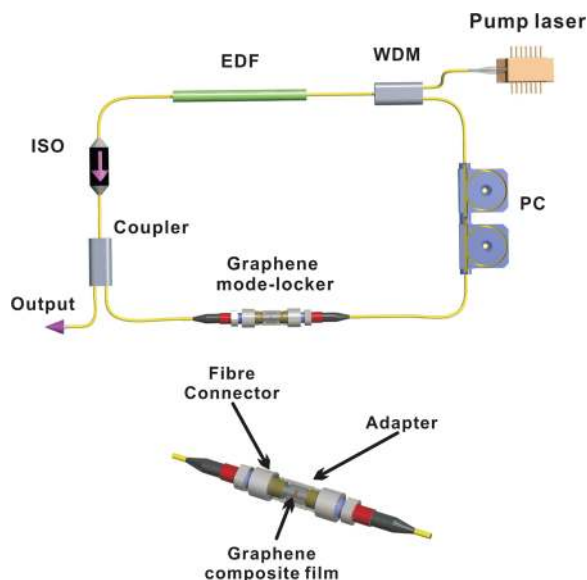


Figure 3. Graphene mode-locked fiber laser and mode-locker assembly. ISO, isolator; WDM, wavelength division multiplexer; PC, polarization controller; EDF, erbium-doped fiber.

$$\begin{aligned} \frac{dn_e}{dt}\bigg|_{\text{pump}} &= \frac{dn_h}{dt}\bigg|_{\text{pump}} = J_{\text{in}} \\ &= \frac{2.2 \times 10^{13} \text{ cm}^{-2}}{0.58 \text{ ps}} = 3.8 \times 10^{13} \text{ cm}^{-2} \text{ ps}^{-1} \end{aligned} \quad (3)$$

This corresponds to pumping the energy at a rate

$$\frac{d\mathcal{E}}{dt}\bigg|_{\text{pump}} = 2J_{\text{in}}\varepsilon_{\text{in}} = 3.0 \times 10^{13} \text{ cm}^{-2} \text{ ps}^{-1} \text{ eV} \quad (4)$$

The electronic energy density \mathcal{E} can be decreased by phonon emission. Neglecting hot phonons, for the Fermi–Dirac distribution (eq 1), the cooling rate can be calculated as (see Methods)

$$\begin{aligned} \frac{d\mathcal{E}}{dt}\bigg|_{\text{ph}} &= -\frac{\lambda_{\Gamma}\omega_{\Gamma}^4}{4\pi v^2} \mathcal{I}(2T_{\text{eff}}/\omega_{\Gamma}) - \frac{\lambda_{\mathbf{K}}\omega_{\mathbf{K}}^4}{4\pi v^2} \mathcal{I}(2T_{\text{eff}}/\omega_{\mathbf{K}}) \\ &\quad - \frac{7\pi^3}{30} L_{\text{ac}} v^2 \left(\frac{T_{\text{eff}}}{v}\right)^5 \end{aligned} \quad (5)$$

$$\mathcal{I}(y) = y^3 \int_0^{\infty} \frac{|x^2 - 1/y^2| dx}{e^{2/y} + 2e^{1/y} \cosh x + 1} \quad (6)$$

The first two terms in eq 5 correspond to emission of optical phonons with wave vectors near Γ and \mathbf{K} , respectively. Their frequencies ω_{Γ} , $\omega_{\mathbf{K}}$ are assumed to be independent of wave vector (Einstein model). The dimensionless coupling constants λ_{Γ} and $\lambda_{\mathbf{K}}$ are defined in ref 33. The third term in eq 5 corresponds to emission of longitudinal acoustic phonons, with frequency taken proportional to their momentum (Debye model). The length L_{ac} in eq 5 is expressed in terms of deformation potential D_0 , carbon atom mass M , and unit cell area A_{uc} as $L_{\text{ac}} = D_0^2 A_{\text{uc}} / (2Mv^3)$. For $D_0 = 10 \text{ eV}$, $A_{\text{uc}} = 5.24 \text{ \AA}^2$, $M = 2.00 \times 10^{-23} \text{ g} = 2.88 \times 10^3 \text{ (eV} \cdot \text{\AA}^2)^{-1}$, $v = 10^8 \text{ cm/s} = 7 \text{ eV} \cdot \text{\AA}$, we obtain $L_{\text{ac}} = 0.26 \times 10^{-3} \text{ \AA}$. We take ω_{Γ}

$= 0.20 \text{ eV}$, $\lambda_{\Gamma} = 0.03$, $\omega_{\mathbf{K}} = 0.15 \text{ eV}$, and $\lambda_{\mathbf{K}} = 0.1$.³⁴ These give the time of optical phonon emission by the photoexcited electron to be $[(\lambda_{\Gamma}/2)(E_L/2 - \omega_{\Gamma}) + (\lambda_{\mathbf{K}}/2)(E_L/2 - \omega_{\mathbf{K}})]^{-1} = 40 \text{ fs}$.³³

From the thermal balance equation

$$\frac{d\mathcal{E}}{dt}\bigg|_{\text{pump}} + \frac{d\mathcal{E}}{dt}\bigg|_{\text{ph}} = 0 \quad (7)$$

we obtain a theoretical estimate $T_{\text{eff}} = 0.20 \text{ eV}$, the dominant contribution to cooling coming from optical phonon emission. Given this T_{eff} and using the Fermi–Dirac distribution (eq 1), we obtain that the absorption of photons with energy $E_L = 0.8 \text{ eV}$ should be reduced by up to $1 + \Delta\alpha_1/\alpha_1 = (1 - f_e)(1 - f_h) = 0.78$. This corresponds to $\Delta\alpha_1/\alpha_1 = -22\%$, while the measured one is -8.2% . Thus, having assumed efficient carrier–carrier relaxation (both intraband and interband) and efficient cooling of the graphene phonons, with the main bottleneck being the transfer of energy from the electrons to the graphene phonons, we obtain a higher saturation level than the measured one. On one hand, this points to other mechanisms contributing to electron cooling (e.g., interaction with the polymer matrix). On the other hand, more importantly, it suggests that sample optimization could lead to enhanced saturable absorption and, thus, much better performance and lower power consumption.

The above estimates are made under the assumption of efficient relaxation due to carrier–carrier collisions, both intraband and interband. However, for linear dispersions near the Dirac point (i.e., for SLG), pair carrier–carrier collisions cannot lead to interband relaxation, thereby conserving the total number of electrons and holes separately. A three-particle collision is required to move an electron from conduction to valence band.^{35,36} Interband relaxation by phonon emission can occur only if the electron and hole energies are close to the Dirac point (within the phonon energy).

Note that for graphite and graphite flakes the situation is completely different: the dispersion near the Dirac point is quadratic, and pair carrier collisions can lead to interband relaxation. Thus, in principle, decoupled graphene monolayers (as in our present experiment, as shown by the FLG Raman spectra) will provide the highest saturable absorption for a given amount of material. To precisely estimate such effect, three-particle collisions would have to be considered. In our case, interband relaxation due to phonon emission seems insufficient to balance the pumping of electrons and holes at the rate given by eq 3 (see Methods). Thus, three-particle collisions do play a role. This is not surprising because the dimensionless Coulomb coupling constant r_s is not very small, and $T_{\text{eff}} = 0.13 \text{ eV}$ is quite high for the corresponding time scale, $(r_s^4 T_{\text{eff}})^{-1}$, to be in the femtosecond range.

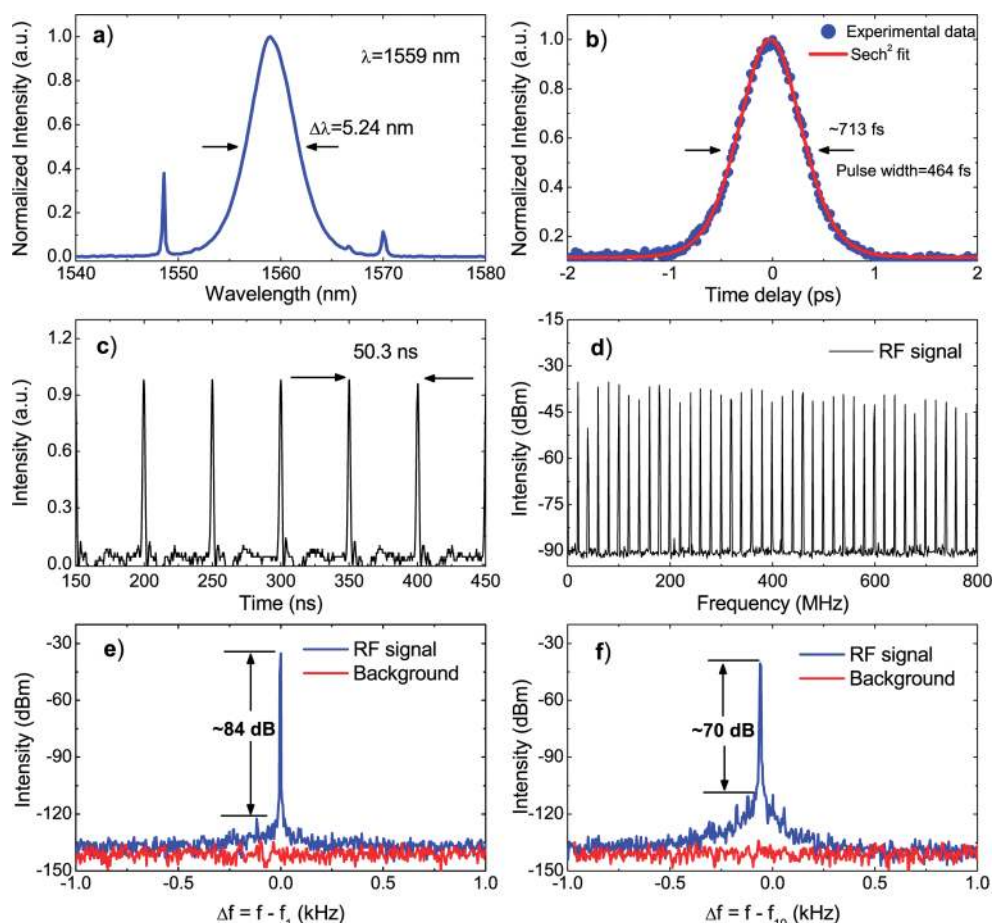


Figure 4. Mode-locked pulses characteristics. (a) Output spectrum; spectral resolution 0.1 nm. (b) Autocorrelation trace of output pulses; delay resolution ~ 20 fs. (c) Oscilloscope trace. (d) Wideband RF spectrum up to 0.8 GHz. (e) RF spectrum measured around the fundamental repetition rate, $f_1 = 19.9$ MHz. (f) RF spectrum measured around the tenth harmonic of the repetition rate, $f_{10} = 199$ MHz. (e,f) Measurement span is 2 kHz with 1 Hz resolution bandwidth. The red trace depicts the background when the laser is switched off.

Ultrafast Laser. We now use our composite to build and test an ultrafast laser working at the main telecommunications window. The mode-locker is assembled by sandwiching the graphene–PVA between two fiber connectors with a fiber adapter, as schematized in Figure 3. A 0.8 m erbium-doped fiber (EDF) is used as the gain medium. It is pumped by a 980 nm diode laser via a wavelength division multiplexer (WDM). An isolator (ISO) is placed after the gain fiber to maintain unidirectional operation. A polarization controller (PC) optimizes mode-locking. A 20/80 coupler is used. The total cavity length is 10.54 m. The input mode diameter is ~ 10 μm .

The threshold pump power for continuous wave lasing is ~ 10 mW. When the pump power is increased to ~ 27 mW, stable mode-locking can be initiated by introducing a disturbance to the intracavity fiber. Once stable output is achieved, no further polarization controller adjustment is needed. It is always possible to decrease the pump power to ~ 22 mW while maintaining mode-locking. When mode-locked, the laser produces a pulse train at a rate of 19.9 MHz.

Figure 4a shows a typical output spectrum, with central wavelength of ~ 1559 nm. The full width at half-maximum (FWHM) bandwidth is 5.24 nm. The side bands at 1548.6 and 1570 nm are typical of soliton-like pulse formation,³⁷ resulting from intracavity periodical perturbations.³⁷ Figure 4b is a second harmonic generation (SHG) autocorrelation trace of the mode-locked pulses after a 50 cm single mode fiber lead from the coupler, with FWHM = 713 fs. Assuming a sech^2 temporal profile, the deconvolution gives a pulse duration of 464 fs. The time bandwidth product (TBP) is 0.3. Due to the autocorrelator delay resolution (20 fs, 5%), there is a minor deviation from 0.315, expected for transform-limited sech^2 pulses, having the shortest duration for a given spectral width. This confirms soliton-like operation.³⁸ Figure 4c is the output pulse train, with a period 50.3 ns, as expected from the fiber cavity length. To study the operation stability, we measure the radio frequency (RF) spectrum. We first perform wide span frequency spectrum measurements up to 800 MHz, as in Figure 4d. This shows no significant spectral modulation, implying no Q-switching instabilities.³⁹ Figure 4e,f

is the RF spectrum around the fundamental repetition rate and its tenth harmonic. A >70 dB peak-to-background ratio (10^7 contrast) is observed, indicating good mode-locking stability.⁴⁰

In the present conditions, for a given wavelength, the performance (in terms of lasing threshold, output power/energy, pulse duration, etc.) of our graphene mode-locked laser is comparable to that previously achieved with SWNTs.^{6–8,10} This is because the laser works in a soliton-like regime due to the interaction of dispersion and nonlinearity. In such regime, pulse shaping is initiated by the saturable absorber. After that, the function of saturable absorber is to stabilize the pulse, and the parameters of the pulse are then mainly determined by other laser cavity properties, such as dispersion.⁴¹ However, wideband operation can be achieved with the as-prepared material, with no need of special procedures, such as the chirality or diameter

selection needed for SWNTs.⁸ Furthermore, all of the graphene flakes contribute in a similar way to the saturable absorption process, unlike the case of SWNTs, where nanotubes not in resonance contribute to the insertion losses. The overall absorption can be simply controlled by the amount of material dispersed in the polymer. Recently, Photoluminescence was detected in oxidized graphene.⁴² This material may also be a convenient saturable absorber, even if the tunability may be lost.

CONCLUSIONS

Our graphene-based ultrafast laser, harnessing the wideband optical nonlinearity of graphene, with no need of band gap engineering, extends the practical potential of this novel material from nanoelectronics to optoelectronics and integrated photonics.

METHODS

Sample Preparation and Characterization. Dispersions are prepared by ultrasonication (Branson 450A, 180 W power, 8–10 °C) 120 mg of graphite (Sigma Aldrich) for 2 h in 10 mL of deionized (DI) water, with 90 mg of sodium deoxycholate (SDC) bile salt. The resulting dispersion is then centrifuged at 5 krpm (2500g) using a TH-641 swing rotor in a Sorvall WX-100 ultracentrifuge for 1 h at 18 °C. The PVA–graphene composite is prepared by mixing 4 mL of the centrifuged dispersion with 2 mL of 15 wt % aqueous PVA (Wako Chemicals) solution in a Hauschild speedmixer (DAC150 FVZ-K) for 5 min at 3 krpm. The mixture is then vacuum evaporated at 20 °C, resulting in a ~50 μm thick composite.

For UV–vis–NIR absorption spectroscopy, 1 part of the centrifuged dispersion is mixed with 10 parts of 0.9 wt % SDC–water solution. The absorption is background subtracted to account for solvent and surfactant. A Perkin-Elmer Lambda 950 UV–vis spectrometer is used. The centrifuged dispersions are diluted and drop-cast onto a Si wafer with 300 nm thermally grown SiO₂. The drops are dried at 20 °C. The samples are then rinsed in acetone for 5 min and water for an additional 5 min. This removes the surfactant. These samples are then used for Raman measurements, collected with a Renishaw 1000 at 514.5 nm using a 100× objective, with an incident power of ~1 mW. For power-dependent transmission measurements, the graphene mode-locker assembly is coupled to a ~580 fs source, tunable from 1548 to 1568 nm, with spectral bandwidth at 1558 nm of 2.8 nm, achieved by filtering a homemade SWNT fiber laser (~400 fs, 38.83 MHz) using a 3 nm band-pass filter. The beam is then amplified by an erbium-doped fiber amplifier and a 20% tap monitors the input power, while 80% is used to pump the graphene mode-locker assembly. Two calibrated power heads read the input/output power simultaneously. The estimated effective mode area on the composite, A_{eff} , is 78.54 μm², deduced from the ~10 μm mode diameter. A spectrum analyzer (Anritsu MS9710B) and a SHG autocorrelator (APE Pulsecheck 50) measure the output spectrum and pulse width, respectively. The RF spectrum is monitored with a lightwave converter connected to a spectrum analyzer.

When the pump wavelength is 1558 nm, the total number of pump photons per cm² per pulse (Γ_{tot}) at 5.35 mW is

$$\Gamma_{\text{tot}} = \frac{5.35 \text{ mW}}{38.83 \text{ MHz} \times E_L \times A_{\text{eff}}} = 1.38 \times 10^{15} \text{ cm}^{-2}$$

As discussed in the main text, the measured transmission of a packaged reference pure PVA device is $\tau_0 = 82.6\%$. Considering the absorption of N graphene layers, $1 - (1 - \alpha_1)^N$, with $\alpha_1 = 2.3\%$, and linear coupling losses, $1 - \tau_0$, to cause the nonsat-

urated loss $1 - \tau$ ($\tau = 65.7\%$), the total number of photons absorbed by the SLG and FLG flakes per cm² per pulse for our maximum pump in the power-dependent absorption measurements is $(82.6 - 65.69\%) \times \Gamma_{\text{tot}} = 2.3 \times 10^{14} \text{ cm}^{-2}$. This can be estimated to be on average equivalent to the effect of ~11 graphene layers: $65.7/82.6 \sim (1 - 2.3\%)^{10.7}$. Then, the average number of photons absorbed per layer per cm² per pulse is $\sim (2.3 \times 10^{14} \text{ cm}^{-2})/11 = 2.2 \times 10^{13} \text{ cm}^{-2}$.

Kinetic Equations. The kinetic equations for the evolution of electron and hole distributions $f_e(\mathbf{p})$, $f_h(\mathbf{p})$ due to phonon emission can be written analogously to ref 33. Here the task is simpler as (i) any spatial dependence is absent; (ii) due to frequent collisions, each photoexcited electron–hole pair is assumed to quickly forget its initial state, so the joint electron–hole distribution function $f(\mathbf{p}, \mathbf{p}')$ factorizes into a product $f_e(\mathbf{p})f_h(\mathbf{p}')$. For $f_{e,h}(\mathbf{p})$ we have

$$\frac{\partial f_e(\mathbf{p})}{\partial t} = \int \frac{v^2 d^2 \mathbf{p}'}{(2\pi)^2} \{ R(\mathbf{p}', \mathbf{p}) f_e(\mathbf{p}') [1 - f_e(\mathbf{p})] - R(\mathbf{p}, \mathbf{p}') f_e(\mathbf{p}) [1 - f_e(\mathbf{p}')] - \tilde{R}(\mathbf{p}, \mathbf{p}') f_e(\mathbf{p}) f_h(\mathbf{p}') \} \quad (8)$$

$$\frac{\partial f_h(\mathbf{p})}{\partial t} = \int \frac{v^2 d^2 \mathbf{p}'}{(2\pi)^2} \{ R(\mathbf{p}', \mathbf{p}) f_h(\mathbf{p}') [1 - f_h(\mathbf{p})] - R(\mathbf{p}, \mathbf{p}') f_h(\mathbf{p}) [1 - f_h(\mathbf{p}')] - \tilde{R}(\mathbf{p}, \mathbf{p}') f_e(\mathbf{p}') f_h(\mathbf{p}) \} \quad (9)$$

The phonons are assumed to be at zero temperature. The intraband relaxation kernel $R(\mathbf{p}, \mathbf{p}')$ is a sum of three terms, corresponding to emission of (i) optical phonons with wave vectors near K , (ii) optical phonons with wave vectors near Γ , and (iii) longitudinal acoustic phonons:

$$R(\mathbf{p}, \mathbf{p}') = R_K(\mathbf{p}, \mathbf{p}') + R_\Gamma(\mathbf{p}, \mathbf{p}') + R_{\text{ac}}(\mathbf{p}, \mathbf{p}') \quad (10)$$

$$R_K(\mathbf{p}, \mathbf{p}') = 2\lambda_K \sin^2 \frac{\varphi_{\mathbf{p}} - \varphi_{\mathbf{p}'}}{2} \pi \delta(v_{\mathbf{p}} - v_{\mathbf{p}'} - \omega_K) \quad (11)$$

$$R_\Gamma(\mathbf{p}, \mathbf{p}') = \lambda_\Gamma \pi \delta(v_{\mathbf{p}} - v_{\mathbf{p}'} - \omega_\Gamma) \quad (12)$$

$$R_{\text{ac}}(\mathbf{p}, \mathbf{p}') = |_{\text{ac}}| \mathbf{p} - \mathbf{p}' | \cos^2 \frac{\varphi_{\mathbf{p}} - \varphi_{\mathbf{p}'}}{2} \pi \delta(v_{\mathbf{p}} - v_{\mathbf{p}'} - v_s |\mathbf{p} - \mathbf{p}'|) \quad (13)$$

The interband kernel contains only the optical phonon contribution:

$$\tilde{R}(\mathbf{p}, \mathbf{p}') = \tilde{R}_K(\mathbf{p}, \mathbf{p}') + \tilde{R}_T(\mathbf{p}, \mathbf{p}') \quad (14)$$

$$\tilde{R}_K(\mathbf{p}, \mathbf{p}') = 2\lambda_K \cos^2 \frac{\varphi_{\mathbf{p}} - \varphi_{\mathbf{p}'}}{2} \pi \delta(\nu p + \nu p' - \omega_K) \quad (15)$$

$$\tilde{R}_T(\mathbf{p}, \mathbf{p}') = \lambda_T \pi \delta(\nu p + \nu p' - \omega_T) \quad (16)$$

Here we use the Einstein model for the optical phonon dispersion (momentum-independent frequencies ω_K, ω_T) and the Debye model for the acoustic phonon dispersion (the frequency of the phonon with wave vector \mathbf{q} is $v_s|\mathbf{q}|$, where $v_s \ll v$ is the sound velocity). We introduce the dimensionless electron–phonon coupling constants λ_K, λ_T for the optical phonons, while the analogous coupling constant for the acoustic phonons has the dimensionality of length since the coupling is proportional to the phonon wave vector:

$$\lambda_T = \frac{F_T^2}{Mv^2\omega_T} \frac{\sqrt{27}a^2}{4}, \quad \lambda_K = \frac{F_K^2}{Mv^2\omega_K} \frac{\sqrt{27}a^2}{4}, \quad (17)$$

$$l_{ac} = \frac{D_0^2}{Mv^2v_s} \frac{\sqrt{27}a^2}{4}$$

Here F_K and F_T are the force constants measuring the change in the electron energy with lattice displacement along the corresponding normal mode (in the nearest-neighbor tight-binding model $F_T = F_K = 3(\partial t_0/\partial a)$, where $\partial t_0/\partial a$ is the derivative of the nearest-neighbor electronic coupling matrix element t_0 with respect to the bond length a), D_0 is the deformation potential, M is the mass of the carbon atom, $[(27^{1/2})a^2]/4$ is the area per carbon atom (half unit cell area). These definitions coincide with those of refs 33 and 34.

For a rigorous treatment of the problem, this kinetic equation should be supplemented with a source term describing the optical pumping of electron and hole populations, as well as electron–electron collision terms for both pair and triple collisions, and then solved. For an estimate, we assume the electron–electron relaxation to be efficient enough to quickly establish the Fermi–Dirac distribution (eq 1) and calculate the cooling rate due to the phonon emission. Combining the definition of \mathcal{E} (eq 2 of the main text) with the kinetic equation, we obtain

$$\left. \frac{d\mathcal{E}}{dt} \right|_{ph} = -4 \int \frac{d^2\mathbf{p}}{(2\pi)^2} \int \frac{v^2 d^2\mathbf{p}'}{(2\pi)^2} W(\mathbf{p}, \mathbf{p}') \quad (18)$$

$$W(\mathbf{p}, \mathbf{p}') = \{f_e(\mathbf{p})[1 - f_e(\mathbf{p}')] + f_h(\mathbf{p})[1 - f_h(\mathbf{p}')]\} \\ \times [\omega_K \tilde{R}_K(\mathbf{p}, \mathbf{p}') + \omega_T \tilde{R}_T(\mathbf{p}, \mathbf{p}') + v_s |\mathbf{p} - \mathbf{p}'| \tilde{R}_{ac}(\mathbf{p} - \mathbf{p}')] \\ + f_e(\mathbf{p})f_h(\mathbf{p}')[\omega_K \tilde{R}_K(\mathbf{p} - \mathbf{p}') + \omega_T \tilde{R}_T(\mathbf{p} - \mathbf{p}')] \quad (19)$$

Substituting here the Fermi–Dirac distribution (eq 1) and calculating the integrals in the approximation $v_s \ll v$, we arrive at eq 5 with $L_{ac} = l_{ac}v_s/v$.

The rate of interband relaxation due to phonon emission is calculated analogously

$$\left. \frac{dn_{e,h}}{dt} \right|_{ph} = -4 \int \frac{d^2\mathbf{p}}{(2\pi)^2} \int \frac{v^2 d^2\mathbf{p}'}{(2\pi)^2} \\ \times f_e(\mathbf{p})f_h(\mathbf{p}')[\tilde{R}_K(\mathbf{p}, \mathbf{p}') + \tilde{R}_T(\mathbf{p}, \mathbf{p}')] \leq \frac{\lambda_T \omega_T^3 + \lambda_K \omega_K^3}{6\pi v^2} \quad (20)$$

We get the upper limit on the relaxation rate by setting $f_e = f_h = 1$. Using the values of the constants given in the main text, we get $9 \times 10^{12} \text{ cm}^{-2} \text{ ps}^{-1}$, four times smaller than the pumping rate in eq 3, thus validating our assumptions.

Acknowledgment. We acknowledge funding from EPSRC/EP/G030480/1, EP/G042357/1 the European Research Council grant NANOPOTS, a Royal Society Brian Mercer Award for Innovation,

the Isaac Newton Trust and the Cambridge Integrated Knowledge Centre in Advanced Manufacturing Technology for Photonics and Electronics. TH acknowledges funding from King's College, Cambridge.

REFERENCES AND NOTES

1. Dausinger, F.; Lichtner, F.; Lubatschowski, H. *Femtosecond Technology for Technical and Medical Applications*; Springer: Berlin, 2004.
2. Keller, U. Recent Developments in Compact Ultrafast Lasers. *Nature* **2003**, *424*, 831.
3. Schütze, K.; Posl, H.; Lahr, G. Laser Micromanipulation Systems as Universal Tools in Cellular and Molecular Biology and in Medicine. *Cell. Mol. Biol.* **1998**, *44*, 735.
4. Xiang, N.; Guina, M. D.; Vainionpää, A. M.; Lyytikäinen, J.; Suomalainen, S.; Saarinen, M. J.; Okhotnikov, O.; Sajavaara, T.; Keinonen, J. Broadband Semiconductor Saturable Absorber Mirrors in the 1.55 μm Wavelength Range for Pulse Generation in Fiber Lasers. *IEEE J. Quantum Electron.* **2002**, *38*, 369.
5. Steinmeyer, G.; Sutter, D. H.; Gallmann, L.; Matuschek, N.; Keller, U. Frontiers in Ultrashort Pulse Generation: Pushing the Limits in Linear and Nonlinear Optics. *Science* **1999**, *286*, 1507.
6. Rozhin, A. G.; Sakakibara, Y.; Namiki, S.; Tokumoto, M.; Kataura, H. Sub-200-fs Pulsed Erbium-Doped Fiber Laser Using a Carbon Nanotube-Polyvinylalcohol Mode Locker. *Appl. Phys. Lett.* **2006**, *88*, 051118.
7. Scardaci, V.; Sun, Z.; Wang, F.; Rozhin, A. G.; Hasan, T.; Hennrich, F.; White, I. H.; Milne, W. I.; Ferrari, A. C. Carbon Nanotube Polycarbonate Composites for Ultrafast Lasers. *Adv. Mater.* **2008**, *20*, 4040.
8. Wang, F.; Rozhin, A. G.; Scardaci, V.; Sun, Z.; Hennrich, F.; White, I. H.; Milne, W. I.; Ferrari, A. C. Wideband-Tuneable, Nanotube Mode-Locked, Fibre Laser. *Nat. Nanotechnol.* **2008**, *3*, 738.
9. Sun, Z.; Rozhin, A. G.; Wang, F.; Hasan, T.; Popa, D.; O'Neill, W.; Ferrari, A. C. A Compact, High-Power, Ultrafast Laser Mode-Locked by Carbon Nanotubes. *Appl. Phys. Lett.* **2009**, *95*, 235102.
10. Hasan, T.; Sun, Z.; Wang, F.; Bonaccorso, F.; Tan, P. H.; Rozhin, A. G.; Ferrari, A. C. Nanotube–Polymer Composites for Ultrafast Photonics. *Adv. Mater.* **2009**, *21*, 3874.
11. Geim, A. K.; Novoselov, K. S. The Rise of Graphene. *Nat. Mater.* **2007**, *6*, 183.
12. Breusing, M.; Ropers, C.; Elsaesser, T. Ultrafast Carrier Dynamics in Graphite. *Phys. Rev. Lett.* **2009**, *102*, 086809.
13. Sun, D.; Wu, Z. K.; Divin, C.; Li, X.; Berger, C.; de Heer, W. A.; First, P. N.; Norris, T. B. Ultrafast Relaxation of Excited Dirac Fermions in Epitaxial Graphene Using Optical Differential Transmission Spectroscopy. *Phys. Rev. Lett.* **2008**, *101*, 157402.
14. Seibert, K.; Cho, G. C.; Kütt, W.; Kurz, H.; Reitze, D. H.; Dadap, J. I.; Ahn, H.; Downer, M. C.; Malvezzi, A. M. Femtosecond Carrier Dynamics in Graphite. *Phys. Rev. B* **1990**, *42*, 2842.
15. Nair, R. R.; Blake, P.; Grigorenko, A. N.; Novoselov, K. S.; Booth, T. J.; Stauber, T.; Peres, N. M. R.; Geim, A. K. Fine Structure Constant Defines Visual Transparency of Graphene. *Science* **2008**, *320*, 1308.
16. Casiraghi, C.; Hartschuh, A.; Lidorikis, E.; Qian, H.; Harutyunyan, H.; Gokus, T.; Novoselov, K. S.; Ferrari, A. C. Rayleigh Imaging of Graphene and Graphene Layers. *Nano Lett.* **2007**, *7*, 2711.
17. Hernandez, Y.; Nicolosi, V.; Lotya, M.; Blighe, F. M.; Sun, Z.; De, S.; McGovern, I. T.; Holland, B.; Byrne, M.; Gun'ko, Y.; et al. High Yield Production of Graphene by Liquid Phase Exfoliation of Graphite. *Nat. Nanotechnol.* **2008**, *3*, 563.
18. Lotya, M.; Hernandez, Y.; King, P. J.; Smith, R. J.; Nicolosi, V.; Karlsson, L. S.; Blighe, F. M.; De, S.; Wang, Z.; McGovern, I. T.; et al. Liquid Phase Production of Graphene by Exfoliation of Graphite in Surfactant/Water Solutions. *J. Am. Chem. Soc.* **2009**, *131*, 3611.

19. Mukerjee, P. Micellar Properties of Drugs: Micellar and Nonmicellar Patterns of Self-Association of Hydrophobic Solutes of Different Molecular Structures-Monomer Fraction, Availability, and Misuses of Micellar Hypothesis. *J. Pharm. Sci.* **1974**, *63*, 972.
20. Bohren, C. F.; Huffman, D. R. *Absorption and Scattering of Light by Small Particles*; Wiley-Interscience: New York, 1998.
21. Abergel, D. S. L.; Fal'ko, V. I. Optical and Magneto-Optical Far-Infrared Properties of Bilayer Graphene. *Phys. Rev. B* **2007**, *75*, 155430.
22. Mak, K. F.; Sfeir, M. Y.; Wu, Y.; Lui, C. H.; Misewich, J. A.; Heinz, T. F. Measurement of the Optical Conductivity of Graphene. *Phys. Rev. Lett.* **2008**, *101*, 196405.
23. Mak, K. F.; Sfeir, M. Y.; Misewich, J. A.; Heinz, T. F. The Electronic Structure of Few-Layer Graphene: Probing the Evolution From a 2-Dimensional to a 3-Dimensional Material. arXiv:0908.0154, 2009.
24. Eberlein, T.; Bangert, U.; Nair, R. R.; Jones, R.; Gass, M.; Bleloch, A. L.; Novoselov, K. S.; Geim, A.; Briddon, P. R. Plasmon Spectroscopy of Free-Standing Graphene Films. *Phys. Rev. B* **2008**, *77*, 233406.
25. Ferrari, A. C.; Meyer, J. C.; Scardaci, V.; Casiraghi, C.; Lazzeri, M.; Mauri, F.; Piscanec, S.; Jiang, D.; Novoselov, K. S.; Roth, S.; et al. Raman Spectrum of Graphene and Graphene Layers. *Phys. Rev. Lett.* **2006**, *97*, 187401.
26. Ferrari, A. C.; Robertson, J. Interpretation of Raman Spectra of Disordered and Amorphous Carbon. *Phys. Rev. B* **2000**, *61*, 14095.
27. Ferrari, A. C.; Robertson, J. Resonant Raman Spectroscopy of Disordered, Amorphous and Diamond-like Carbon. *Phys. Rev. B* **2001**, *64*, 075414.
28. Tuinstra, F.; Koenig, J. L. Raman Spectrum of Graphite. *J. Chem. Phys.* **1970**, *53*, 1126.
29. Casiraghi, C.; Hartschuh, A.; Qian, H.; Piscanec, S.; Georgi, C.; Fasoli, A.; Novoselov, K. S.; Basko, D. M.; Ferrari, A. C. Raman Spectroscopy of Graphene Edges. *Nano Lett.* **2009**, *9*, 1433.
30. Latil, S.; Meunier, V.; Henrard, L. Massless Fermions in Multilayer Graphitic Systems With Misoriented Layers: *Ab Initio* Calculations and Experimental Fingerprints. *Phys. Rev. B* **2007**, *76*, 201402(R).
31. Kampfrath, T.; Perfetti, L.; Schapper, F.; Frischkorn, C.; Wolf, M. Strongly Coupled Optical Phonons in the Ultrafast Dynamics of the Electronic Energy and Current Relaxation in Graphite. *Phys. Rev. Lett.* **2005**, *95*, 187403.
32. Lazzeri, M.; Piscanec, S.; Mauri, F.; Ferrari, A. C.; Robertson, J. Electron Transport and Hot Phonons in Carbon Nanotubes. *Phys. Rev. Lett.* **2005**, *95*, 236802.
33. Basko, D. M. Theory of Resonant Multiphonon Raman Scattering in Graphene. *Phys. Rev. B* **2008**, *78*, 125418.
34. Basko, D. M.; Piscanec, S.; Ferrari, A. C. Electron–Electron Interactions and Doping Dependence of the Two-Phonon Raman Intensity in Graphene. *Phys. Rev. B* **2009**, *80*, 165413.
35. González, J.; Guinea, F.; Vozmediano, M. A. Unconventional Quasiparticle Lifetime in Graphite. *Phys. Rev. Lett.* **1996**, *77*, 3589.
36. Foster, M. S.; Aleiner, I. L. Slow Imbalance Relaxation and Thermoelectric Transport in Graphene. *Phys. Rev. B* **2009**, *79*, 085415.
37. Dennis, M. L.; Duling, I. N. Experimental Study of Sideband Generation in Femtosecond Fiber Lasers. *IEEE J. Quantum Electron.* **1994**, *30*, 1469.
38. Agrawal, G. P. *Applications of Nonlinear Fiber Optics*; Academic Press: San Diego, CA, 2001.
39. Honninger, C.; Paschotta, R.; Morier-Genoud, F.; Moser, M.; Keller, U. Q-Switching Stability Limits of Continuous-Wave Passive Mode Locking. *J. Opt. Soc. Am. B* **1999**, *16*, 46.
40. Von der Linde, D. Characterization of the Noise in Continuously Operating Mode-Locked Lasers. *Appl. Phys. B: Laser Opt.* **1986**, *39*, 201.
41. Keller, U. Ultrafast Solid-State Lasers. In *Progress in Optics*; Elsevier: Amsterdam, 2004; Vol. 46.
42. Gokus, T.; Nair, R. R.; Bonetti, A.; Bohmler, M.; Lombardo, A.; Novoselov, K. S.; Geim, A. K.; Ferrari, A. C.; Hartschuh, A. Making Graphene Luminescent by Oxygen Plasma Treatment. *ACS Nano* **2009**, *3*, 3963.